PHYSICAL REVIEW E **108**, 064412 (2023)

Biphasic amplitude oscillator characterized by distinct dynamics of trough and crest

Jun Jin,[1,*] Fei Xu,[2,*] Zhilong Liu,[1] Hong Qi,[3] Chenggui Yao,[4] Jianwei Shuai,[1,5] and Xiang Li[1,†]
[1]*Department of Physics, Xiamen University, Xiamen, Fujian 361005, China*
[2]*Department of Physics, Anhui Normal University, Wuhu, Anhui 241002, China*
[3]*Complex Systems Research Center, Shanxi University, Taiyuan, Shanxi 030006, China*
[4]*College of Data Science, Jiaxing University, Jiaxing, Zhejiang 314000, China*
[5]*Oujiang Laboratory (Zhejiang Lab for Regenerative Medicine, Vision and Brain Health) and Wenzhou Institute, University of Chinese Academy of Sciences, Wenzhou, Zhejiang 325001, China*

(Received 14 July 2023; accepted 28 November 2023; published 26 December 2023)

Biphasic amplitude dynamics (BAD) of oscillation have been observed in many biological systems. However, the specific topology structure and regulatory mechanisms underlying these biphasic amplitude dynamics remain elusive. Here, we searched all possible two-node circuit topologies and identified the core oscillator that enables robust oscillation. This core oscillator consists of a negative feedback loop between two nodes and a self-positive feedback loop of the input node, which result in the fast and slow dynamics of the two nodes, thereby achieving relaxation oscillation. Landscape theory was employed to study the stochastic dynamics and global stability of the system, allowing us to quantitatively describe the diverse positions and sizes of the Mexican hat. With increasing input strength, the size of the Mexican hat exhibits a gradual increase followed by a subsequent decrease. The self-activation of input node and the negative feedback on input node, which dominate the fast dynamics of the input node, were observed to regulate BAD in a bell-shaped manner. Both deterministic and statistical analysis results reveal that BAD is characterized by the linear and nonlinear dependence of the oscillation trough and crest on the input strength. In addition, combining with computational and theoretical analysis, we addressed that the linear response of trough to input is predominantly governed by the negative feedback, while the nonlinear response of crest is jointly regulated by the negative feedback loop and the self-positive feedback loop within the oscillator. Overall, this study provides a natural and physical basis for comprehending the occurrence of BAD in oscillatory systems, yielding guidance for the design of BAD in synthetic biology applications.

DOI: 10.1103/PhysRevE.108.064412

I. INTRODUCTION

Oscillatory signals are ubiquitous in various biological systems ranging from bacteria, fungi, to humans [1–4]. These signals are involved in numerous physiological processes, such as cellular metabolism, cell division, hormone secretion, circadian rhythm, heartbeat, muscle contraction, and so on [5–12]. These processes are regulated by biological oscillators [13], which exhibit diverse oscillatory features to play essential roles in gene regulation [14], protein expression [15], or stimuli transduction [16]. Biological systems have been observed to frequently exhibit a nonmonotonic response to input strength [17–20]. In oscillatory systems, it has been widely reported in experiments that amplitude presents a biphasic response to the strength of stimuli. Chen *et al.* [21] found that emodin can bidirectionally regulate the contractility of jejunal smooth muscle. Kaur *et al.* [22] and Chavan *et al.* [23] observed that the amplitude of phosphorylated KaiC and KaiB first increases and then decreases with the increase of KaiA concentration. Jeong *et al.* [24] also reported that the amplitude of KaiC phosphorylation oscillation is biphasically regulated by magnesium ions. Møller *et al.* [25] showed that the effect of the magnetic flux density on the O_2-oscillation amplitude is biphasic in peroxidase-oxidase reaction. Biphasic behaviors related to oscillation amplitude have also been observed in neurophysiology signals [26–28]. Recently, Liu *et al.* [29] showed that the degradation rate of frq mRNA could biphasically regulate its amplitude through the circadian negative feedback loop.

To explore how complex behaviors emerge from biological networks, a large number of theoretical and experimental studies have been performed. Recent studies suggested that core motifs play a crucial role in determining the properties of biological function, despite the presence of dozens of components and interactions in networks [30–32]. Various motifs that perform specific biological functions have been widely determined, including reliable cell decision [33], faithful noise resistance [34], robust biological oscillations [35–39], optimal fold-change detection [40,41], cell adaptation [42], cell polarization [43], cell fate decision [44–48], and dual function of adaptation and noise attenuation [49]. In addition to identifying key motifs, the regulation and free-energy consumption of specific biological functions was also extensively investigated. For example, incoherent inputs were found that can enhance

---

[*] These authors contributed equally to this work.
[†] Corresponding author: xianglibp@xmu.edu.cn

the robustness of biological oscillators [31]. Oberreiter *et al.* [50] conjectured a universal bound to answer the question of the minimum amount of free-energy consumption required for a certain number of coherent oscillations. The dissociation constant was also demonstrated to biphasically regulate oscillation amplitude in a protein-protein interaction network [51].

As an essential biological behavior, how the properties of the biphasic amplitude dynamics (BAD) of oscillation are characterized by specific structure and components remains unclear. Here, we aimed to demonstrate the design principles of BAD in natural systems. Through searching all possible two-node topologies, we determined the core oscillators that enable robust oscillation and identified relaxation oscillation as the essential mechanism. From the viewpoint of landscape, the stochastic dynamic and global stability of the BAD controlled by the input strength was investigated. Further analysis reveals the mechanism behind the BAD is linear and nonlinear dependence of the oscillation trough and crest on input strength. Overall, these findings provide better understanding and theoretical guidance for the design of the diverse oscillatory behaviors in synthetic biology applications.

II. MODEL AND METHOD

To investigate the network topology capable of achieving BAD of oscillation, we considered a two-node system (X,Y). Node X receives external signals, while node Y transmits the system's output. The dynamics of the system can be described by the following two coupled ordinary differential equations (ODEs):

$$\frac{dX}{dt} = F_1(X, Y) = I(1 - X) + F_{XX} + F_{YX} - k_{\text{inh}X}X, \tag{1}$$

$$\frac{dY}{dt} = F_2(X, Y) = F_{XY} + F_{YY} - k_{\text{inh}Y}Y, \tag{2}$$

where

$$F_{MN} = \begin{cases} k_i M \frac{(1-N)^n}{J_i^n + (1-N)^n}\ , & M \text{ activates } N \\ 0\ , & \text{no interaction} \\ -k_i M \frac{N^n}{J_i^n + N^n}, & M \text{ inhibits } N. \end{cases} ,\quad M, N \in \{X, Y\}$$

The first term on the right-hand side of Eq. (1) represents the activation term of X induced by external input signal I. The last terms on the right-hand side of Eqs. (1) and (2) correspond to the self-inactivation of X and Y, respectively. In Eqs. (1) and (2), the rest terms on the right-hand side represent the feedback action of M on N, denoted as F_{MN} (M,$N \in \{X,Y\}$). There are four feedback interactions in total (i.e., F_{XX}, F_{XY}, F_{YX}, and F_{YY}). The total amount of each species is normalized to 1, giving the inactivation amount of species N to be $1-N$. The Hill equation has been widely employed for describing multistep, complicated, or not fully understood reaction processes [44,52]. If variable M activates variable N, the inactivation amount of variable N is $1-N$, which is then activated by M. Thus, the Hill term $k_i M \frac{(1-N)^n}{J_i^n+(1-N)^n}$ was employed to describe the positive feedback effect of M on N. Conversely, if variable M inhibits variable N, it means that the activation amount of species N will be inhibited. In this case, the Hill term $-k_i M \frac{N^n}{J_i^n+N^n}$ was used to indicate the negative feedback effect of M on N. n denotes the Hill coefficient, k_i denotes the feedback strength, and J_i denotes the Michaelis-Menten constant.

The phenomenological model was developed based on well-established approaches used in previous studies [36,42,43], with the variables normalized in equations. The two nodes can represent different signal transducers under specific biological conditions. For the extracellular inputs signal, node X could represent the receptors on the cell membrane for receiving inputs, while node Y represents the downstream proteins recruited by the receptors. In the case of the intracellular inputs signal, node X serves as the signal transducer for activating node Y, which could be the effector proteins. Additionally, the two nodes can also represent the regulatory relationship between two genes in the nucleus. The unit of the two variables is an arbitrary unit.

A Latin hypercube sampling method [53] is employed to randomly scan the model parameters in the wide parameter space for evaluating the robust oscillation behavior of the systems. The input signal strength I is in the range of 0–1. k_i, the rate constant for activation or inhibition, is in the range of 10^{-1}–10^{3}. J_i, the Michaelis-Menten constant, is in the range of 10^{-3}–10^{1}. k_{inh}, the rate constant of inactivation, is in the range of 10^{-3}–10^{1}. The Hill coefficient n_i is a random integer sampling with 1–4. All the parameters and Hill coefficient n_i of the model are sampled within the proper ranges based on previous studies [31,42].

To check whether the output oscillation signals are truly effective and robust, the criteria are defined as follows [31,45]:

$$(H1){:}\frac{\text{std}(Y_i)}{\text{mean}(Y_i)} < 10^{-2}, \qquad \frac{\text{std}(t_{i+1} - t_i)}{\text{mean}(t_{i+1} - t_i)} < 10^{-2},$$

$$(H2){:}\frac{Y_{\max} - Y_{\min}}{\text{maximum expression amount}} > 0.01,$$

where t_i and Y_i represent the moment when the ith peak occurs and its output signal, respectively. mean and std represent the value of mean and standard deviation, respectively. In ($H2$), $Y_{\max}$ represents the maximum value of the output signal, corresponding to the oscillation crest. $Y_{\min}$ represents the minimum value of the output, corresponding to the oscillation trough. We used the odeint function in the Scipy library to simulate the mathematical model. The evolution time of the system under any set of parameters ranges from 0 to 5000 min. The sampled systems require at least five consecutive peaks to meet the conditions ($H1$) and ($H2$).

Biochemical reactions in natural systems are usually influenced by intrinsic or external fluctuations [54,55]. The stochastic dynamics can be described by a Langevin equation, i.e., $dC_i(t)/dt = F_i(C) + \eta_i(t)$, where C_i represents the concentration of species. $F_i(C)$ represents the driving force that describes the dynamics of the system. The term $\eta_i(t)$ represents fluctuation or noise force, which obeys Gaussian distribution with correlation function $\langle \eta_i(t)\eta_j(t')\rangle = 2D_{\text{ij}}\delta_{\text{ij}}\delta(t-t')$, where δ_{ij} is the Dirac delta function and D is the diffusion coefficient matrix characterizing the strength of the fluctuations. Here, we assumed the isotropic and homogeneous case $D_{11} = D_{22}$. The probability evolution P for the system can be reflected by the Fokker-Planck equation

$$\frac{\partial P(C,t)}{\partial t} = -\sum_i \frac{\partial}{\partial C_i}[F_i(C)P(C,t)] + \sum_i D_i \frac{\partial^2}{\partial C_i^2} P(C,t). \tag{3}$$

The global steady-state probability distribution P_{ss} of the state space can be obtained by solving the steady-state solution of the above Fokker-Planck equation. The corresponding dimensionless potential U can be calculated by the Boltzmann relation, $U = -\ln(P_{ss})$.

III. RESULTS

A. Three out of nineteen topologies can exhibit oscillatory behavior

The procedure for searching oscillatory behavior in a two-node system is illustrated in Fig. 1(a). In our model, the interaction F_{XY} between X and Y in Eq. (2), where X is the input node and Y is the output node, is fixed as an activation process [left panel of Fig. 1(a)]. Hence, taking into account three possible interaction scenarios (activation, inhibition, or no interaction) for each of the three remaining interactions (F_{XX}, F_{YX}, and F_{YY}) in Eqs. (1) and (2), there are $3^3 = 27$ kinds of topologies in total for the two-node system. Previous studies have demonstrated that the existence of at least one negative feedback loop is the necessary condition to produce robust oscillation [10,35,56,57]. We further ruled out eight topologies without any negative feedback loop. Thus, there are 19 possible oscillatory topologies in two-node networks [Fig. 1(b)].

To determine whether a topology can achieve robust oscillation, we generated 10^6 sets of randomly selected parameters for each topology using a Latin hypercube sampling method, within the meaningful parameter space [31,42] [Fig. 1(a)]. For sampling uniformity, we used logarithmic sampling for parameters k_i, J_i, and k_{inh}, and linear sampling for parameter I. $Y_{\max}$ represents the maximum value of the output node, which corresponds to the oscillation crest. $Y_{\min}$ represents the minimum value of the output, which corresponds to the oscillation trough [right panel in Fig. 1(a)]. We recorded the set number among 10^6 tests for each topology and detected oscillation dynamics. From the time series of X and Y in Fig. 1(b), we observed that only three topologies (i.e., M10, M14, and M19) can generate robust oscillation and their corresponding oscillation probabilities (OSC prob.) are shown in Fig. 1(c). It can be observed that topology M10 exhibits the highest oscillation probability, followed by M14 and M19. It is suggested that the addition of autoregulation at node Y will reduce the probability of oscillation for M10.

Next, we aimed to investigate why the remaining 16 topologies are not capable of generating robust oscillations. Firstly, for topologies M1, M2, M3, M4, M5, M6, M9, M12, M13, and M15, which have no self-activation for both nodes X and Y, choosing a Dulac function $B(X,Y) = 1$, we have

$$\begin{aligned}\frac{\partial(BF_1)}{\partial X} + \frac{\partial(BF_2)}{\partial Y} &= -I - k_{\text{inh}X} - k_{\text{inh}Y} + \frac{\partial F_{XX}}{\partial X} + \frac{\partial F_{YX}}{\partial X} + \frac{\partial F_{XY}}{\partial Y} + \frac{\partial F_{YY}}{\partial Y} \\ &= -I - k_{\text{inh}X} - k_{\text{inh}Y} - k_3 X \frac{n_3(1-Y)^{n_3-1}J_3^{n_3}}{\left[(1-Y)^{n_3} + J_3^{n_3}\right]^2} + \frac{\partial F_{XX}}{\partial X} + \frac{\partial F_{YX}}{\partial X} + \frac{\partial F_{YY}}{\partial Y},\end{aligned} \tag{4}$$

where the interaction

$$\begin{aligned} F_{XX} &= 0 \text{ or } -k_1 X \frac{X^{n_1}}{X^{n_1} + J_1^{n_1}}, \\ F_{YX} &= 0,\ -k_2 Y \frac{X^{n_2}}{X^{n_2} + J_2^{n_2}} \text{ or } k_2 Y \frac{(1-X)^{n_2}}{(1-X)^{n_2} + J_2^{n_2}}, \\ F_{YY} &= 0 \text{ or } -k_4 Y \frac{Y^{n_4}}{Y^{n_4} + J_4^{n_4}}. \end{aligned} \tag{5}$$

The following Lemma 1 is needed as well:

$$\begin{aligned} &\frac{d}{dx}\left(\frac{x^n}{x^n + J^n}\right) = \frac{nx^{n-1}J^n}{(x^n + J^n)^2}, \quad \frac{d}{dx}\left(\frac{x^{n+1}}{x^n + J^n}\right) = \frac{x^{2n} + (n+1)x^n J^n}{(x^n + J^n)^2}, \\ &\frac{d}{dx}\left(\frac{(1-x)^n}{(1-x)^n + J^n}\right) = -\frac{n(1-x)^{n-1}J^n}{[(1-x)^n + J^n]^2}, \quad \frac{d}{dx}\left(\frac{1}{x}\frac{(1-x)^n}{(1-x)^n + J^n}\right) = -\frac{nx(1-x)^{n-1}J^n + (1-x)^n[(1-x)^n + J^n]}{[(1-x)^n + J^n]^2 x^2}. \end{aligned} \tag{6}$$

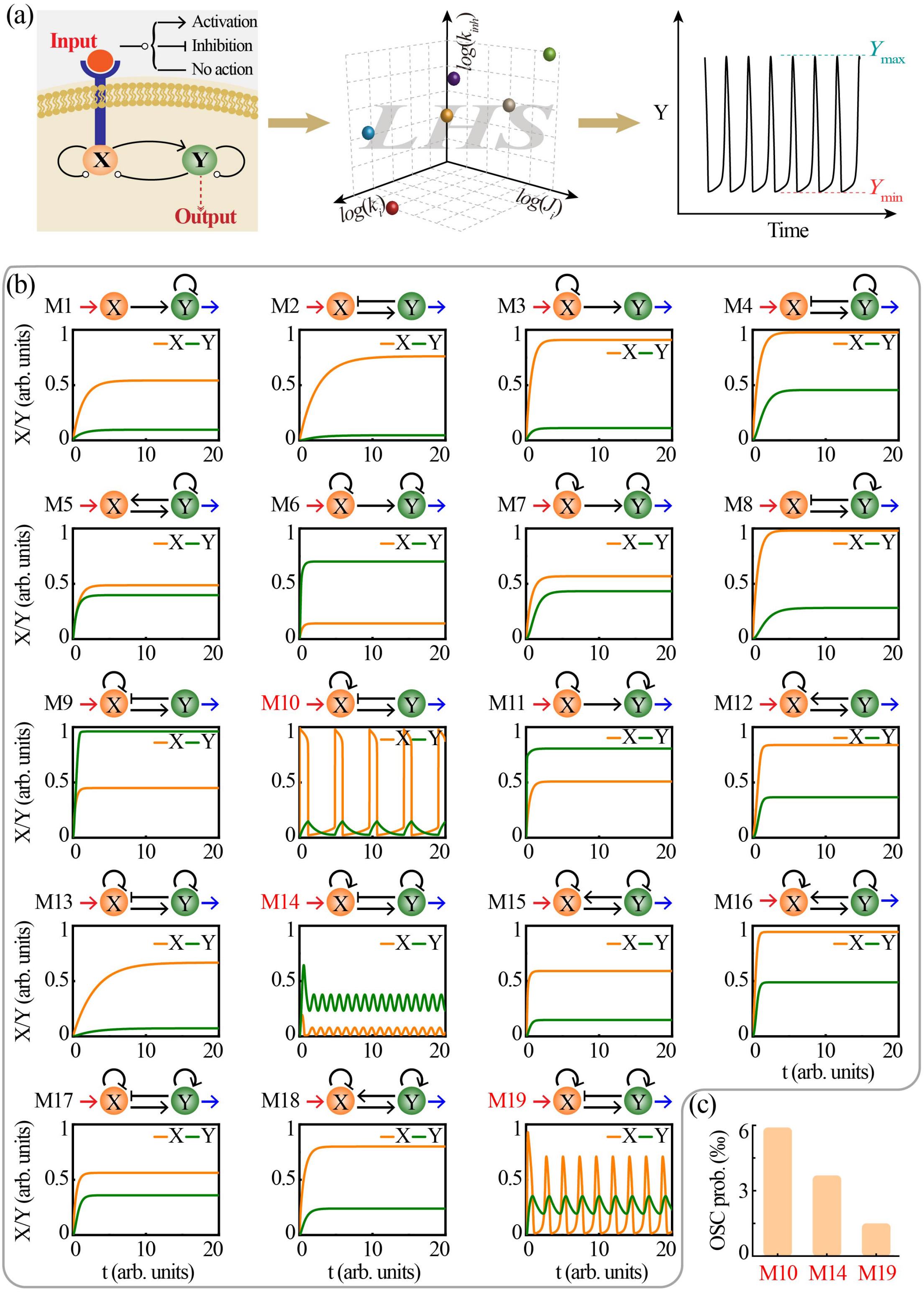

FIG. 1. Identifying the core oscillator in two-node systems with random circuit analysis. (a) Schematic of the workflow. Left panel: enumeration of topologies with two nodes. Node X is used to receive the input signals and node Y is the output. Middle panel: stochastic analysis of the Latin hypercube sampling procedure is used to produce random parameter sets for each topology. Right panel: The robust oscillation signal of the node Y is detected numerically. $Y_{\max}$ and $Y_{\min}$ are the oscillation crest and trough of Y, respectively. (b) Time series of a representative deterministic model for each of the 19 possible topologies, M1–M19. (c) Probabilities of parameter sets that yield robust oscillations for the topologies of M10, M14, and M19.

Substituting Eq. (5) into Eq. (4) and applying Lemma 1, it yields

$$\frac{\partial(BF_1)}{\partial X} + \frac{\partial(BF_2)}{\partial Y} < 0.$$

Then, for topologies M8, M11, M17, and M18, which have self-activation only for node Y, choosing a Dulac function $B(X, Y) = 1/Y$, we have

$$\begin{aligned}\frac{\partial(BF_1)}{\partial X} + \frac{\partial(BF_2)}{\partial Y} &= -\frac{I + k_{\text{inh}X}}{Y} + \frac{\partial}{\partial X}\left(\frac{F_{XX}}{Y}\right) + \frac{\partial}{\partial X}\left(\frac{F_{YX}}{Y}\right) + \frac{\partial}{\partial Y}\left(\frac{F_{XY}}{Y}\right) + \frac{\partial}{\partial Y}\left(\frac{F_{YY}}{Y}\right)\\ &= -\frac{I + k_{\text{inh}X}}{Y} - k_3 X\frac{n_3 Y(1-Y)^{n_3-1}J_3^{n_3} + (1-Y)^{n_3}\left[(1-Y)^{n_3} + J_3^{n_3}\right]}{\left[(1-Y)^{n_3} + J_3^{n_3}\right]^2 Y^2}\\ &\quad - k_4\frac{n_4(1-Y)^{n_4-1}J_4^{n_4}}{\left[(1-Y)^{n_4} + J_4^{n_4}\right]^2} + \frac{1}{Y}\frac{\partial F_{XX}}{\partial X} + \frac{\partial}{\partial X}\left(\frac{F_{YX}}{Y}\right),\end{aligned} \tag{7}$$

where the interaction

$$\begin{aligned}F_{XX} &= 0 \quad \text{or} \quad -k_1 X\frac{X^{n_1}}{X^{n_1} + J_1^{n_1}},\\ F_{YX} &= 0, -k_2 Y\frac{X^{n_2}}{X^{n_2} + J_2^{n_2}} \quad \text{or} \quad k_2 Y\frac{(1-X)^{n_2}}{(1-X)^{n_2} + J_2^{n_2}}.\end{aligned} \tag{8}$$

Substituting Eq. (8) into Eq. (7) and applying Lemma 1, it yields

$$\frac{\partial(BF_1)}{\partial X} + \frac{\partial(BF_2)}{\partial Y} < 0.$$

Finally, for topologies M7 and M16, which have self-activation only for node X, choosing a Dulac function $B(X, Y) = 1/X$, we have

$$\begin{aligned}\frac{\partial(BF_1)}{\partial X} + \frac{\partial(BF_2)}{\partial Y} &= -\frac{I}{X^2} - \frac{k_{\text{inh}Y}}{X} + \frac{\partial}{\partial X}\left(\frac{F_{XX}}{X}\right) + \frac{\partial}{\partial X}\left(\frac{F_{YX}}{X}\right) + \frac{\partial}{\partial Y}\left(\frac{F_{XY}}{X}\right) + \frac{\partial}{\partial Y}\left(\frac{F_{YY}}{X}\right)\\ &= -\frac{I + k_{\text{inh}Y}X}{X^2} - \frac{k_1 n_1(1-X)^{n_1-1}J_1^{n_1}}{\left[(1-X)^{n_1} + J_1^{n_1}\right]^2} - \frac{k_3 n_3(1-Y)^{n_3-1}J_3^{n_3}}{\left[(1-Y)^{n_3} + J_3^{n_3}\right]^2} - k_4\frac{Y^{2n_4} + (n_4+1)Y^{n_4}J_4^{n_4}}{X(Y^{n_4} + J_4)^2} + \frac{\partial}{\partial X}\left(\frac{F_{YX}}{X}\right),\end{aligned} \tag{9}$$

where the interaction

$$F_{YX} = 0 \text{ or } k_2 Y\frac{(1-X)^{n_2}}{(1-X)^{n_2} + J_2^{n_2}}. \tag{10}$$

Substituting Eq. (10) into Eq. (9) and applying Lemma 1, it also yields

$$\frac{\partial(BF_1)}{\partial X} + \frac{\partial(BF_2)}{\partial Y} < 0.$$

Hence, according to the Bendixson-Dulac criterion [58], these 16 topologies have no periodic solutions and cannot generate oscillation.

B. Relaxation oscillation determined by the fast and slow dynamics of the two nodes

After identifying the three oscillators, the next aim is to explore the control mechanism behind the generation of these oscillation behaviors. The probability distributions for the parameters related to the interactions are shown in Fig. 2(a), revealing that oscillations are more easily observed in certain parameter regions. The probability distributions for the same parameters of the three oscillators (M10, M14, and M19) exhibit consensus features. Specifically, the rate constant k_1, which characterizes the process of self-activation of X, tends to be at an intermediate value to promote the occurrence of oscillation. The rate constant k_2, representing the inhibition strength of X by Y, tends to be large. Moreover, the interaction strengths of X activating Y (k_3) and the self-action of Y (k_4) are typically small.

The probability distribution of k_2 is generally large, indicating that the process of Y inhibiting X occurs rapidly. A small value of k_3 and k_4 suggests weak interaction strengths on Y, potentially leading to a slow dynamics of Y. Although k_1 (self-activation of X) tends to be at an intermediate value, k_1 is more than 100 times greater than k_3 and k_4. This also confirms that the self-activation of X is a rapid process compared to the dynamics of Y. Three representative dynamics of X and Y, individually selected from the three oscillators (M10, M14, and M19), are displayed in the top panel of Fig. 2(b). These dynamics intuitively illustrate the fast and slow oscillation dynamics of X and Y. To quantify the fast/slow dynamics, we further employed the ratio of the full width at half maximum (FWHM [59]) to the oscillation period. The ratio falls within the open interval of (0,1), and a smaller value indicates faster

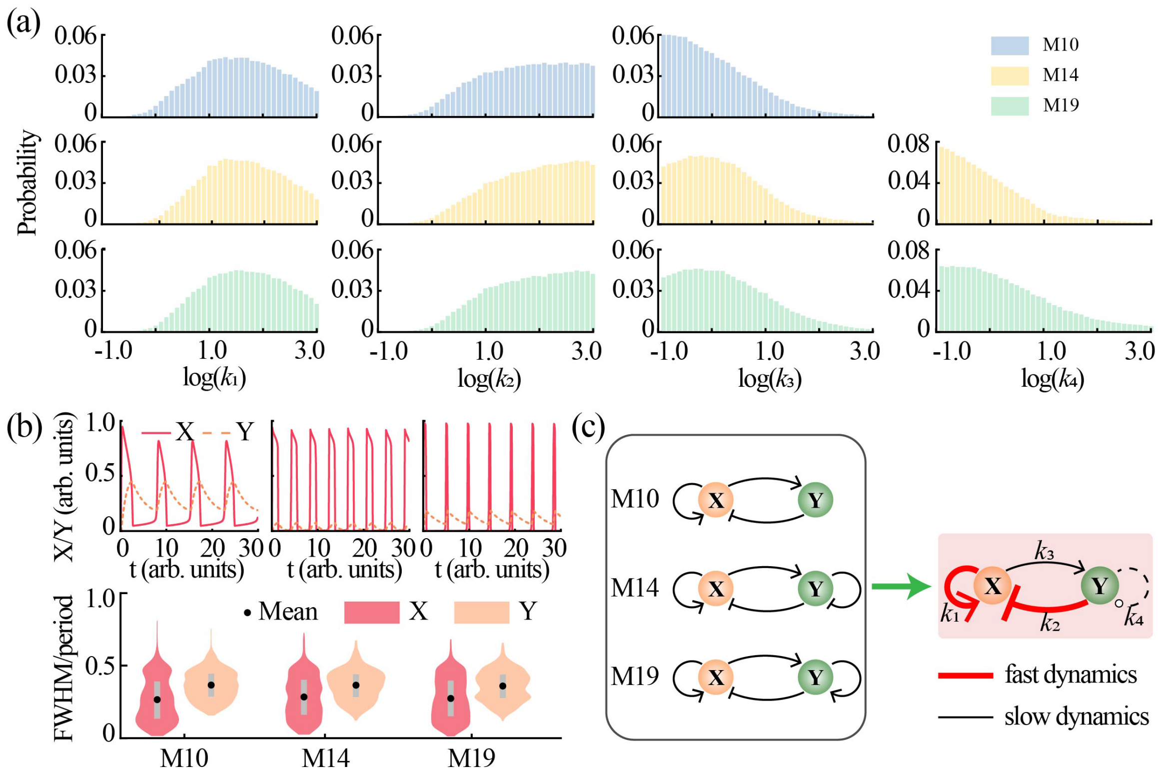

FIG. 2. Identification of the essence for oscillation in two-node oscillators. (a) Parameter distributions of all the identified deterministic models that can produce oscillation in topologies M10, M14, and M19. (b) Three representative time series of nodes X and Y selected from oscillators M10, M14, and M19 (top panels), along with the violin plot of the ratio, which is defined as FWHM/period of nodes X and Y (bottom panels). The top and bottom of the gray box denote the 75th and 25th percentiles, respectively. The black point within the gray box represents the mean value. The peripheral curve of the violin plot describes the probability density distribution, and also the maximum and minimum values. (c) The schematic diagram of the essence of three oscillators. Here, the dynamics of activator X is significantly faster than repressor Y. The thick red lines indicate the fast dynamics, and the thin black line indicates the slow dynamics. The dashed-line circle indicates the self-action of node Y that may be activation, inhibition, or absent.

dynamic. As depicted in the bottom panel of Fig. 2(b), the statistical results indicate that these three oscillators share a common feature, confirming that the dynamics of X are significantly faster than Y.

Hence, these three oscillators are characterized by the same core structure [Fig. 2(c)]. The self-activation of X and the inhibition of X by Y, represented by the thick red lines, dominate the fast dynamics of X. The activation of Y by X, represented by the thin black line, determines the slow dynamics of Y. This specific type of oscillation is classified as a relaxation oscillation. It is characterized by a limit cycle that involves a slow and gradual buildup, followed by a sudden discharge, and then another slow buildup, and so on [60].

C. BAD induced by distinct responses of trough and crest, from a global stability viewpoint

Having determined the core structure and essence for oscillation, we next sought to explore how the properties of BAD of oscillation are characterized. Due to its core structure and the highest probability for oscillation among the three topologies (M10, M14, and M19), M10 was chosen as a representative example topology for further analysis. For simplification, we initially randomly selected a deterministic model parameter set of Eq. (11) that satisfied the criterion of BAD with topology M10, as shown below:

$$\begin{aligned}\frac{dX}{dt} &= I(1-X) + 1.49 * X\frac{1-X}{1-X+0.04}\\ &\quad - 1.36 * Y\frac{X^2}{X^2+0.0014^2} - 0.003 * X,\\ \frac{dY}{dt} &= 0.93 * X\frac{(1-Y)^3}{(1-Y)^3} + 0.04^3 - 0.34 * Y. \qquad (11)\end{aligned}$$

As the results show in Fig. 3(a), the amplitude of Y is biphasically regulated by the input strength. The coefficient H, which is defined as $H = (Y_{\mathrm{peak}} - Y_{\mathrm{ES}})/Y_{\mathrm{tot}}$ to quantify the scale of BAD. Y_{peak} refers to the highest level of amplitude reached by Y, while Y_{ES} represents the amplitude of Y under the maximum input strength. Y_{tot} is the total amount of node Y. The three representative time series of the system's oscillation are displayed in Fig. 3(b). The results highlight that as input strength increases, both trough and crest exhibit an upward trend, but the amplitude initially increases and then decreases, resulting in the occurrence of BAD.

To systematically study the stochastic properties of M10 oscillation, the generalized potential landscape [61,62] that describes the global dynamic behavior of the system in phase space is employed. The dimensionless potential U and the

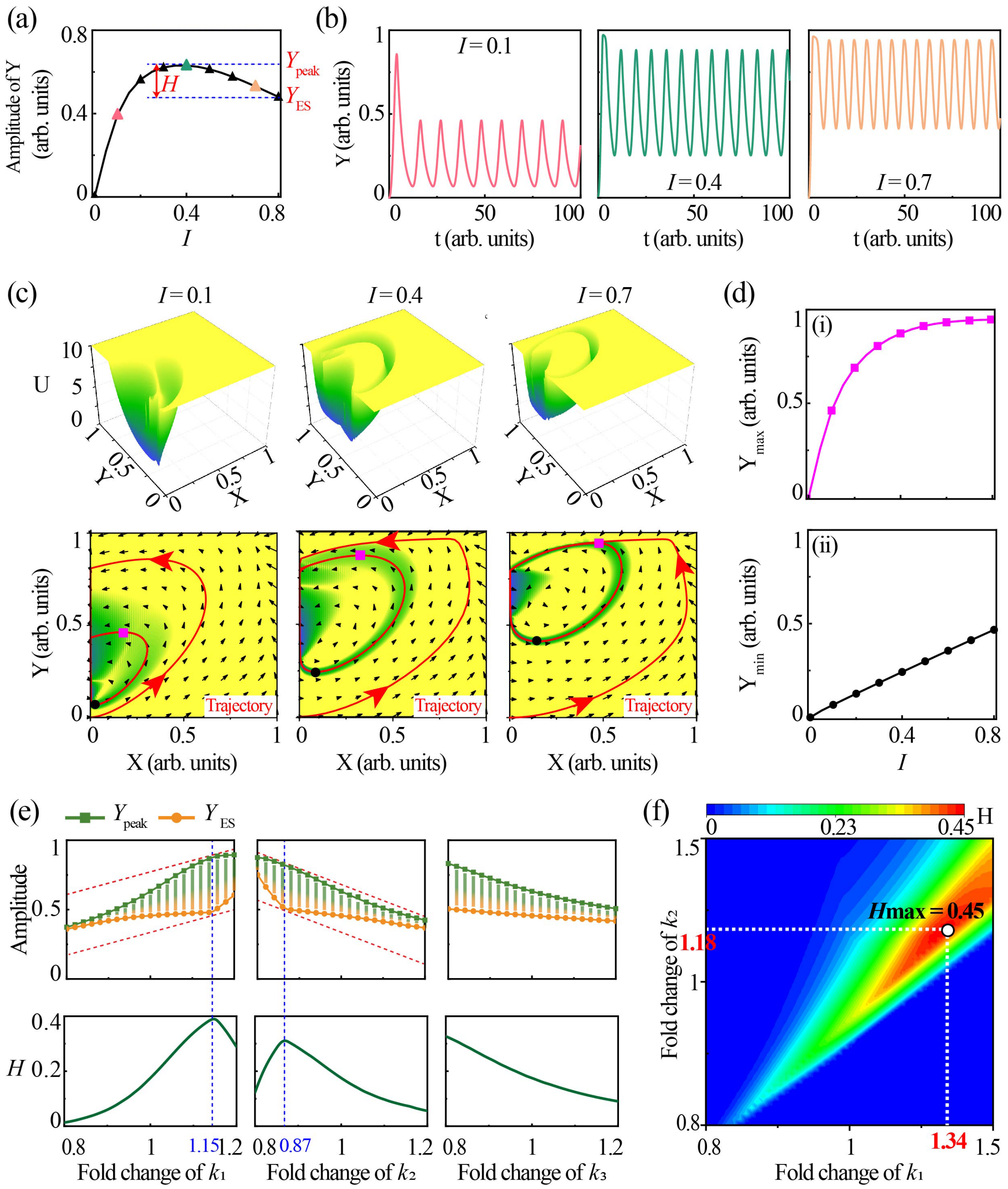

FIG. 3. A concrete example of a deterministic model of topology M10 to characterize BAD of oscillation. (a) The variation of oscillation amplitude Y with input I increases in a deterministic oscillation model. (b) Time series of Y when $I = 0.1$, 0.4, and 0.7 in the deterministic oscillation model. (c) The potential landscape of the system when $I = 0.1$, 0.4, and 0.7, respectively (top panels), and the corresponding vertical views of the landscapes (bottom panels). The vector field is indicated by the black arrows. The trajectories with red arrows show that the solutions converge to a limit-cycle oscillation after initial transient. The oscillation crest and trough of Y in the trajectories are represented by magenta squares and black circles, respectively. (d) Crest $Y_{\max}$ and trough $Y_{\min}$ of Y change as the increase of input I. € Analysis of the core parameters k_1, k_2, and k_3 in regulating H/BAD. (f) Phase diagram of H in $k_1 - k_2$ parameter spaces.

steady-state probability distribution P_{ss} of the system are given by the Boltzmann relation, i.e., $U = -\ln(P_{ss})$. The potential landscapes that mapped onto the X-Y phase space under three typical input strengths are shown in Fig. 3(c). The yellow region represents higher potential or lower probability, and the blue region represents lower potential or higher probability.

The system consistently exhibits Mexican hat landscapes under various input strengths [top panels in Fig. 3(c)]. The system evolves into a unique annular valley from any initial values, indicating that there is a unique limit cycle in the X-Y phase space under certain input strength. As the red trajectories show in the bottom panels in Fig. 3(c), the system will

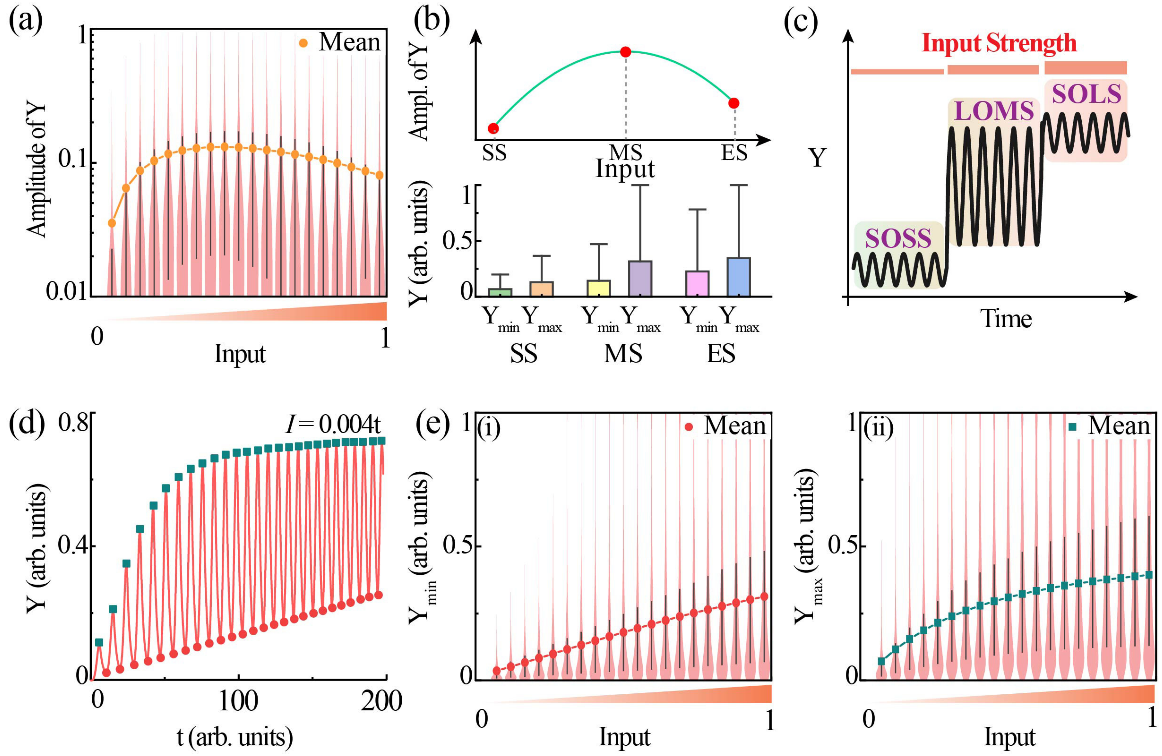

FIG. 4. Statistical analysis of 10^4 deterministic models that satisfy the criterion of BAD for topology M10. (a) The distributions of oscillation amplitude of Y under different input strength. (b) Bar chart of the oscillation crest Y_{max} and trough Y_{min} at oscillation-starting stimulus (SS), medium stimulus strength (MS), and oscillation-ending stimulus (ES) for topology M10, respectively (bottom panels). (c) Different oscillation behaviors of Y in response to different input strengths. SOSS, small oscillation at small stimulus strength; LOMS, large oscillation at medium stimulus strength; SOLS, small oscillation at large stimulus strength. (d) A special case to illustrate the time courses of Y responding to input with the intensity $I = 0.004t$. (e) The violin plots of statistical results of oscillation crest Y_{max} and trough Y_{min} on more than 10^4 parameter sets of topology M10, respectively. The mean of the trough Y_{min} increase linearly with the increasing stimulation intensity, while the mean of the crest Y_{max} increase nonlinearly.

eventually evolve into the ring trap oscillation after an initial transient. The vector field is indicated by the black arrows. The differences among these landscapes under different input strength lie in the positions and sizes of the Mexican hat. With increasing input strength, the size of the limit cycles exhibits a gradual increase followed by a subsequent decrease [bottom panels in Fig. 3(c)]. This modulation indicates that the amplitude is biphasically regulated by the input strength. Then, the oscillation crest (magenta squares) and trough (black circles) of Y on the limit cycle were calculated. As shown in Fig. 3(d), as the input strength increases, the oscillation trough Y_{min} exhibits a linear increase, while the oscillation crest Y_{max} demonstrates a nonlinear growth that eventually saturates. The distinct responses of oscillation trough and crest to changes in input strength serve as triggers for the emergence of BAD. To minimize the dependence on a specific deterministic model with particular parameters, we randomly selected another deterministic oscillation model parameter set that met the criterion of BAD. Similar dynamics, topological landscapes, and conclusions were also observed (see Supplemental Material, Fig. S1 [63]).

The role of interaction terms in mediating BAD was investigated as well. Among the three interaction terms in M10 [Fig. 2(c)], the self-activation of X (k_1) and the inhibition of X by Y (k_2) that dominate the fast dynamics of X, can both mediate the amplitude of Y_{peak} and Y_{ES}, resulting in a bell-shaped regulation on BAD [Fig. 3(e)]. The activation of Y by X (k_3), which governs the slow dynamics of Y, only exerts a negative influence on the amplitude of Y_{peak}. As a result, k_3 negatively regulates BAD. Further two-parameters phase plane analysis indicates that the maximum value of H is 0.45 when the fold change of k_1 and k_2 is 1.34 and 1.18, respectively [Fig. 3(f)]. The above results underscore the interactions (k_1 and k_2) that dominate the fast dynamics of X, are functionally significant for diversely regulating BAD of oscillation.

D. BAD characterized by linear and nonlinear responses of trough and crest, from a statistical viewpoint

To mitigate the influence of specific parameters and minimize fortuitous outcomes associated with deterministic models, a statistical analysis is conducted to delve into the underlying mechanism of BAD of oscillation. We collected more than 10^4 parameter sets that satisfy the criterion of BAD using topology M10. The violin plots in Fig. 4(a) depict the distributions of Y amplitude across various input strengths. Consistent with the results of the deterministic model [Fig. 3(a)], the plots reveal that the mean value of amplitudes exhibit a biphasic curve as the input strength increases.

The minimal input strength required to initiate oscillation is referred to as the oscillation-starting stimulus (SS), whereas the maximum input strength that leads to the termination of oscillation is named as the oscillation-ending stimulus (ES) [top panel in Fig. 4(b)]. The medium stimulus strength is short for MS. Statistical analysis suggests that as the input strength increases, both the levels of oscillation trough and crest exhibit an upward trend [bottom panel in Fig. 4(b)]. Quantitatively, the results reveal that the input-dependent oscillation topology transitions from small oscillation at small stimulus strength (SOSS) to large oscillation at medium stimulus strength (LOMS), and then back to small oscillation at large stimulus strength (SOLS) [Fig. 4(c)].

We further decomposed the amplitude Y into the difference between the oscillation crest and trough. To provide a visual representation of the BAD in the time series, we have plotted a specific example in Fig. 4(d). As the stimulus gradually increases over time ($I = 0.004t$), the trough of Y (red circles) exhibits a linear increase, whereas the crest (dark-cyan squares) shows a nonlinear growth pattern. This is a general phenomenon, as confirmed by the violin plots of crest $Y_{\max}$ and trough $Y_{\min}$ shown in Fig. 4(e). Based on these statistical results of BAD, we determined that the mean value of the trough $Y_{\min}$ (red circles) linearly increases with the input strength, whereas the mean value of the crest $Y_{\max}$ (dark-cyan squares) exhibits a nonlinear increase. The linear and nonlinear responses of trough and crest to stimulus intensity were also respectively observed for M14 and M19 (see Supplemental Material, Fig. S2 [63]), revealing that our conclusion regarding the mechanisms behind the BAD of oscillation is general.

E. Linear response of trough to input strength dominated by the negative feedback of *Y* to *X*

Our subsequent objective was to investigate the underlying mechanism responsible for the linear increase of the oscillation trough with the input strength. The dynamics of the system in topology M10 are governed by the following two coupled ODEs:

$$\frac{dX}{dt} = I(1-X) + k_1 X \frac{(1-X)^{n_1}}{(1-X)^{n_1} + J_1^{n_1}} - k_2 Y \frac{X^{n_2}}{X^{n_2} + J_2^{n_2}} - k_{\mathrm{inh}X} X, \tag{12}$$

$$\frac{dY}{dt} = k_3 X \frac{(1-Y)^{n_3}}{(1-Y)^{n_3} + J_3^{n_3}} - k_{\mathrm{inh}Y} Y. \tag{13}$$

We collected more than 10^4 parameter sets that satisfy the criterion of BAD. For these parameter sets, it was observed that the majority of the values for term $(1 - Y_{\min})^{n_3}/[(1 - Y_{\min})^{n_3} + J_3^{n_3}]$ are close to 1 [Fig. 5(a) and Fig. S3(a) in the Supplemental Material [63]].

Given the simplification of term $(1-Y)^{n_3}/[(1-Y)^{n_3} + J_3^{n_3}]$ to approximately 1 in our analysis, when Y takes the value of oscillation trough $Y_{\min}$, its derivatives are equal to 0. Thus, near $t = T_{Y\min}$, the form of Eq. (13) can be reduced as follows:

$$k_3 X - k_{\mathrm{inh}Y} Y = 0,$$

that is,

$$Y = \frac{k_3}{k_{\mathrm{inh}Y}} X. \tag{14}$$

Thus, the oscillation trough $Y_{\min}$ can be approximated as $k_3 * X\_Y_{\min}/k_{\mathrm{inh}Y}$, where $X\_Y_{\min}$ represents the value of X when Y takes $Y_{\min}$. To validate this deduction, we counted $X\_Y_{\min}$ under different input strengths. The violin distributions presented in Fig. 5(b) confirm that the mean of $X\_Y_{\min}$ approximately exhibits a linear increase with increasing input strength. Consequently, the question of why the oscillation trough $Y_{\min}$ increases linearly with the input strength can be reframed as a question of why $X\_Y_{\min}$ increases linearly with input strength.

We integrated the information flows of each term on the right-hand side of Eq. (12) over the interval $[T_{X\min}, T_{Y\min}]$ to investigate their contributions to the dynamics of X [Fig. 5(c)]. It is shown that terms $k_1 X \frac{(1-X)^{n_1}}{(1-X)^{n_1}+J_1^{n_1}}$ and $k_{\mathrm{inh}X} X$ have negligible contributions to X compared to terms $I(1-X)$ and $k_2 Y \frac{X^{n_2}}{X^{n_2}+J_2^{n_2}}$ [Fig. 5(d) and Fig. S3(b) in the Supplemental Material [63]]. Ignoring the two terms $k_1 X \frac{(1-X)^{n_1}}{(1-X)^{n_1}+J_1^{n_1}}$ and $k_{\mathrm{inh}X} X$, substituting Eq. (14) into Eq. (12), and simplifying the term $\frac{X\_Y_{\min}^{n_2}}{X\_Y_{\min}^{n_2}+J_2^{n_2}}$ to 1 [Fig. 5(e) and Fig. S3(c) in the Supplemental Material [63]], we can derive an approximate equation of X:

$$\frac{dX}{dt} = I(1-X) - \frac{k_2 k_3}{k_{\mathrm{inh}Y}} X, \tag{15}$$

with initial value $(T_{X\min}, X_{\min})$. Solving Eq. (15), we obtained

$$X = I\left(\left(I + {}^{k_2 k_3}\!/_{k_{\mathrm{inh}Y}}\right)^{-1} + \left(X_{\min} - I\left(I + {}^{k_2 k_3}\!/_{k_{\mathrm{inh}Y}}\right)^{-1}\right) \Big/ I e^{-(I+\frac{k_2 k_3}{k_{\mathrm{inh}Y}})(t - T_{X\min})}\right). \tag{16}$$

When t is equal to $T_{Y\min}$, we have

$$X\_Y_{\min} = I\left(\left(I + {}^{k_2 k_3}\!/_{k_{\mathrm{inh}Y}}\right)^{-1} + \left(X_{\min} - I\left(I + {}^{k_2 k_3}\!/_{k_{\mathrm{inh}Y}}\right)^{-1}\right) \Big/ I e^{-(I+\frac{k_2 k_3}{k_{\mathrm{inh}Y}}) * PD}\right), \tag{17}$$

where PD is the phase difference between X and Y. We further calculated the ratio of the first term to the second term in the parentheses of Eq. (17) and defined it as K. The probability distribution shows that the value of K is larger than 10 for more than 90% of the parameter sets [Fig. 5(f) and Fig. S3(d) in the Supplemental Material [63]], indicating that the first term dominates over the second term in a significant majority of cases. Thus, Eq. (17) can be reduced to

$$X\_Y_{\min} = \frac{I}{I + {}^{k_2 k_3}\!/_{k_{\mathrm{inh}Y}}}. \tag{18}$$

Subsequently, we examined the distribution of $k_2 k_3/k_{\mathrm{inh}Y}$. As shown in Fig. 5(g), $k_2 k_3/k_{\mathrm{inh}Y}$ exceeds 1 in more than 98% of the parameter sets, with more than 82% of the parameter sets surpassing 5. Comparing with $k_2 k_3/k_{\mathrm{inh}Y}$, $I \in [0, 1]$ is

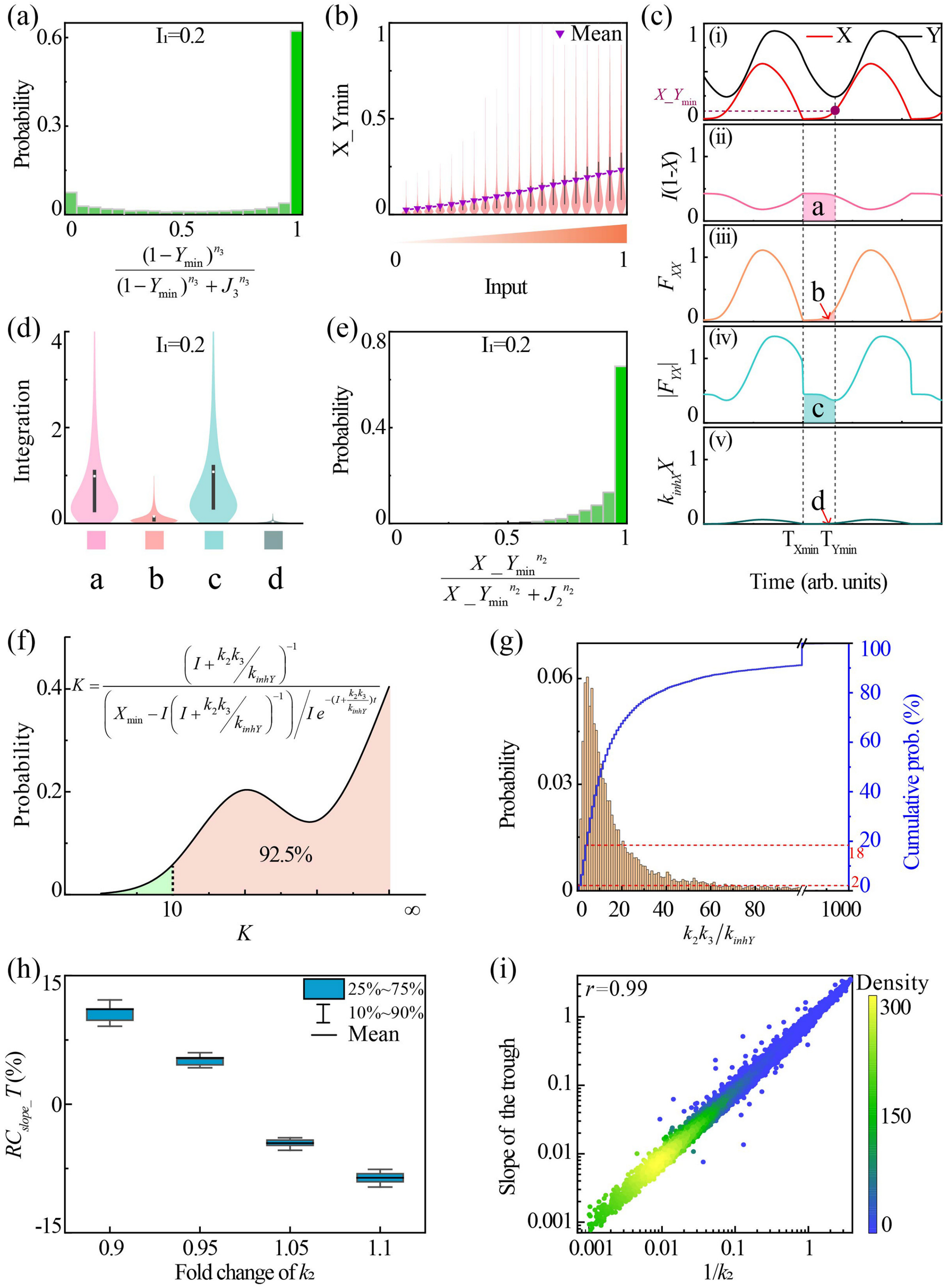

FIG. 5. Mechanism analysis of the linear response of the oscillation trough to the input strength. (a) The probability distribution of term $(1-Y_{\min})^{n_3}/[(1-Y_{\min}]^{n_3}+J_3^{n_3})$ at $I = 0.2$. (b) The violin plots of $X\_Y_{\min}$ under different input strengths. (c) Schematic diagrams of dissecting the influences of each term on $X\_Y_{\min}$. (d) The violin plots for the area marked with a, b, c, and d in Fig. 5(c), respectively. (e) The probability distribution of term $X\_Y_{\min}^{n2}/(X\_Y_{\min}^{n2}+J_2^{n2})$, showing that most of the values are equal to 1. (f) The probability distribution of K. (g) The probability distribution of $k_2k_3/k_{\text{inh}Y}$. The left-Y axis indicates probability (bar plot) and the right-Y axis presents the cumulative probability (blue line plot). (h) The change of $RC_{\text{slope}\_}T$ (variation of the slope of oscillation trough) with the fold change of k_2. (i) Comparison of slope of the oscillation trough calculated by simulation and theoretical value $1/k_2$ with more than 10^4 parameter sets of topology M10. Pearson correlation coefficient $r = 0.99$.

negligibly small. Thus, Eq. (18) can be further simplified as follows:

$$X\_Y_{\min} = \frac{k_{\mathrm{inh}Y}}{k_2 k_3} I. \tag{19}$$

Substituting Eq. (19) into Eq. (14), we derived

$$Y_{\min} = \frac{k_3}{k_{\mathrm{inh}Y}} X\_Y_{\min} = \frac{k_3}{k_{\mathrm{inh}Y}} \frac{k_{\mathrm{inh}Y}}{k_2 k_3} I \approx \frac{1}{k_2} I. \tag{20}$$

Ultimately, we established the approximate relationship between the strength of input I and the trough of Y. The slope of the trough is primarily determined by the reciprocal of the negative feedback of Y to X, which is represented by $1/k_2$.

To test the conclusion of the above theoretical analysis, single-parameter sensitivity is conducted for the interaction parameters in topology M10. The change rate of slope (RC_{slope}) is defined as follows:

$$RC_{\mathrm{slope}} = \frac{\mathrm{slope}_{\mathrm{var}} - \mathrm{slope}_{\mathrm{sta}}}{\mathrm{slope}_{\mathrm{sta}}} * 100\%, \tag{21}$$

where $\mathrm{slope}_{\mathrm{sta}}$ refers to the slope obtained under the standard parameter value, while $\mathrm{slope}_{\mathrm{var}}$ is the slope obtained after the parameter changes. As the statistical results show in Fig. 5(h), k_2 exhibits a clear negative linear correlation with the slope of the oscillation trough (RC_{slope_T}), while the other parameters have negligible influences compared to k_2 [see Supplemental Material, Fig. S3(e) [63]]. Furthermore, we calculated the slope of the oscillation trough with each parameter set and observed that their Pearson correlation coefficients with the theoretical value of $1/k_2$ exceeds 0.99 [Fig. 5(i)].

F. Nonlinear response of crest to input strength jointly governed by the core interactions

We next tried to explore the nonlinear response of oscillation crest $Y_{\max}$ to input strength. Similarly, for these collected 10^4 parameter sets that satisfy the criterion of BAD, it was observed that the majority of the values for term $(1-Y_{\max})^{n_3}/[(1-Y_{\max})^{n_3} + J_3^{n_3}]$ are close to 1 in Eq. (13) [Fig. 6(a) and Fig. S4(a) in the Supplemental Material [63]]. We thus simplified the term $(1-Y)^{n_3}/[(1-Y)^{n_3} + J_3^{n_3}]$ to 1 in our analysis. Then, the oscillation crest $Y_{\max}$ has a linear relationship with its corresponding X (i.e., $X\_Y_{\max}$) based on Eq. (14). Statistical results confirm that $X\_Y_{\max}$ also exhibits a nonlinear increase with increasing input strength [Fig. 6(b)].

Subsequently, we also integrated the information flows of each term on the right-hand side of Eq. (12) in the interval $[T_{Y\min}, T_{Y\max}]$ to investigate their influences on $X\_Y_{\max}$ [Fig. 6(c)]. As the results show [Fig. 6(d) and Fig. S4(b) in the Supplemental Material [63]], the term $k_{\mathrm{inh}X}X$ is negligibly small and has little contribution to $X\_Y_{\max}$ compared with the terms $I(1-X)$, $k_1 X \frac{(1-X)^{n_1}}{(1-X)^{n_1}+J_1^{n_1}}$ and $k_2 Y \frac{X^{n_2}}{X^{n_2}+J_2^{n_2}}$. Ignoring term $k_{\mathrm{inh}X}X$, substituting the linear relationship between $X\_Y_{\max}$ and $Y_{\max}$ into Eq. (12), and approximating term $\frac{X\_Y_{\max}^{n_2}}{X\_Y_{\max}^{n_2}+J_2^{n_2}}$ to 1 [Fig. 6(e) and Fig. S4(c) in the Supplemental Material [63]], the following equation of X in the small interval $[T_{Y\min}, T_{Y\max}]$ can be obtained:

$$\frac{dX}{dt} = I(1-X) + k_1 X \frac{(1-X)^{n_1}}{(1-X)^{n_1} + J_1^{n_1}} - k_2 \frac{k_3}{k_{\mathrm{inh}Y}} X. \tag{22}$$

Compared with Eq. (15), Eq. (22) exhibits strong nonlinearity, making it difficult for both theoretical analysis and finding approximate solutions. Thus, we conducted parameter sensitivity analysis to numerically identify the interactions that have a major impact on the oscillation crest under varying input strengths. By varying each rate parameter in topology M10, including the self-activation of X (k_1), the inhibition of X by Y (k_2), the activation of Y by X (k_3), the inactivation of X ($k_{\mathrm{inh}X}$), and the inactivation of Y ($k_{\mathrm{inh}Y}$) by ±5% and ±10%, the relative percentage change of the slope of the oscillation crest at the oscillation-starting stimulus ($RC_{\mathrm{slope}\_}SS$) and the oscillation-ending stimulus ($RC_{\mathrm{slope}\_}ES$) was recorded. The sensitivity spectrums for these parameters are depicted in Figs. 6(f) and 6(g).

Figure 6(f) shows that an increase of k_1 significantly shifts the distribution position of $RC_{\mathrm{slope}\_}SS$ upwards, while an increase in k_2 and k_3 shifts the distribution position downwards. Changes in $k_{\mathrm{inh}X}$, and $k_{\mathrm{inh}Y}$ do not have a significant influence on the distribution position. This indicates that the oscillation crest around the oscillation-starting stimulus is positively regulated by the self-activation rate of X (k_1) and negatively regulated by the inhibition of X by Y (k_2) and the activation of Y by X (k_3). The interactions related to k_1, k_2, k_3, and $k_{\mathrm{inh}Y}$ have great influences on the oscillation crest around the oscillation-ending stimulus [Fig. 6(g)]. The different trends observed in the distributions between Figs. 6(f) and 6(g) suggest that each interaction has an opposite effect on the slope of the crest at the oscillation-starting stimulus compared to the oscillation-ending stimulus. Therefore, the above analysis confirms that the oscillation crest to input strength are jointly determined by the core interactions. The interplay between these interactions contributes to the observed nonlinear behavior of the crest and further shapes the BAD of oscillation in the system.

IV. DISCUSSION

Biological oscillators are considered a fundamental characteristic of vital movement, regulating important physiological functions such as the cell cycle, circadian rhythm, and embryonic development [64–66]. In addition, biphasic behavior, characterized by distinct phases or responses, is observed in various biological processes including cell differentiation, proliferation, and death [67–69]. While the regulatory mechanisms of oscillation and biphasic behavior have been extensively studied in different biological systems, the characterization of BAD of oscillation remains unclear. The goal of this study is to find the minimal topological structures that can generate BAD of oscillation and dissect the underlying design principles. Firstly, stochastic analysis of a Latin hypercube sampling method was used to search two-node topologies that can realize oscillation, the prerequisite of BAD. We generated 10^6 sets of randomly selected model parameters for each of the 19 possible topologies, and found that only three topologies, M10, M14, and M19 can robustly oscillate with probabilities of 5.9‰, 3.7‰, and 1.5‰, respectively [Fig. 1(c)]. To avoid omitting topologies capable of generating robust oscillation in numerical simulations, we theoretically derived a general conclusion using the Bendixson-Dulac theorem: the remaining 16 topologies cannot generate oscillation, regardless of parameter choices. To clearly illustrate the

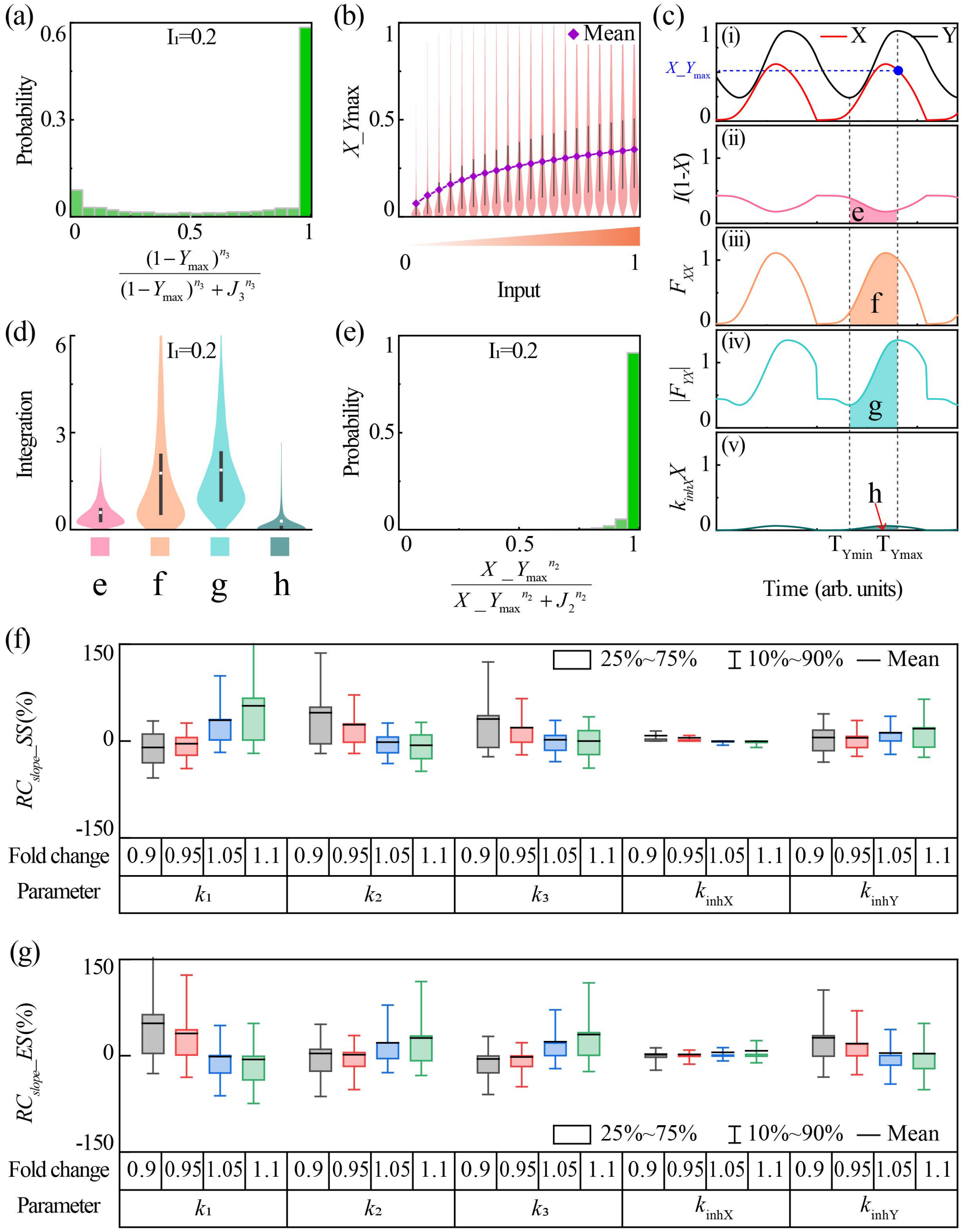

FIG. 6. Analysis of the nonlinear response of the oscillation crest to the input strength. (a) The probability distribution of term $(1-Y_{\max})^{n_3}/[(1-Y_{\max})^{n_3}+J_3^{n_3}]$ at $I=0.2$. (b) The violin plots of $X\_Y_{\max}$ under different input strengths. (c) Schematic diagrams of dissecting the influences of each term on $X\_Y_{\max}$. (d) The violin plots for the areas marked with e, f, g, and h in Fig. 6(c), respectively. (e) The probability distribution of term $X\_Y_{\max}^{n2}/(X\_Y_{\max}^{n2}+J_2^{n2})$, showing that most of the values are equal to 1. (f) and (g) The changes of RC_{slope}_SS (variation rate of the slope of the oscillation crest at the oscillation-start stimulus) and (variation rate of the slope of the oscillation crest at the oscillation-ending stimulus) with the fold change of each parameter.

aforementioned results, we selected a specific set of model parameters for each topology as a representative example, and their corresponding time series are shown in Fig. 1(b). Then, by individually calculating the parameter distributions of all the identified deterministic models that can produce oscillations in topologies M10, M14, and M19 [Fig. 2(a)], we arrived at a general conclusion: oscillations in these three topologies are characterized by the same core structure [Fig. 2(c)], which governs the fast and slow dynamics of the two signal nodes [Fig. 2(b)]. Using a deterministic model of the core structure M10, which can induce BAD by the input, we found a special result: with the increase of input intensity, the oscillation trough increases linearly, and the crest rises nonlinearly. This leads to an initial increase and subsequent decrease in amplitude, resulting in the occurrence of BAD (Fig. 3). To achieve a more general conclusion, we collected more than 10^4 sets of model parameters, i.e., 10^4 deterministic models for topology M10 that satisfy the criterion of BAD (Fig. 4). Statistical analysis of all these 10^4 deterministic models confirms that the linear and nonlinear responses of the oscillation trough and crest to input are the general physical mechanism for BAD dynamics [Fig. 4(e)]. Finally, combining statistical analysis of these 10^4 deterministic models with theoretical analysis, we determined that the physical mechanisms behind BAD dynamics are as follows: the linear response of the trough to input is governed by the negative feedback of the output node on the input node (Fig. 5), while the nonlinear response of the crest is jointly dominated by the negative feedback loop and the self-positive feedback loop on the input node (Fig. 6).

Studies on several biological oscillators such as cell death, cell cycles, and quorum sensing, have shown that only a limited number of topologies are capable of robustly executing oscillation [45,70,71]. Through searching all possible two-node topologies, we determined that only three topologies can exhibit oscillatory behavior. These three oscillators are characterized by the same core structure, including a negative feedback loop between two nodes and a self-positive feedback loop of the input node. This is supported by the previous findings that although a negative feedback loop is necessary for oscillation, it alone is not sufficient [35,72]. The presence of an additional positive feedback loop, which can induce a delay kinetic [35,72], is crucial for robust oscillation. Similar core structures for generating oscillation have been observed in studies on cell death signaling and quorum sensing signaling [45,70]. Besides focusing on the core structure, the functional role of auxiliary structures in oscillators has also been highlighted. For example, Li *et al.* validated that the robustness of biological oscillators is enhanced by the incoherent inputs [31]. Recently, the design principle for robust oscillatory behaviors with respect to noise has also been demonstrated [73]. Here, our result demonstrated that adding a self-positive or self-negative feedback loop of the output node to the core structure (M14 or M19) significantly reduces the probability of oscillation [Fig. 1(c)]. This observation suggests that robust oscillators are obtained by augmenting the number of both negative feedback loops and positive self-regulations while maintaining an appropriate balance between positive and negative interactions [74].

Positive and negative feedback loops are crucial for the generation and regulation of oscillation. Previous findings by Zhang *et al.* highlighted that the p53-Mdm2 and ATM-p53-Wip1 negative feedback loops are responsible for p53 pulses, while the switchlike behaviors of p53 manifest when the p53-PTEN-Akt-Mdm2 positive feedback loop becomes dominant [75]. Besides, their work revealed that enhancing the positive feedback can either promote or suppress oscillations, depending on the strength of both feedback loops, emphasizing the crucial role of the interplay between positive and negative feedback in the transitions between oscillation and bistability [76]. Natural selection may favor a robust network structure. While analyzing two topologically equivalent genetic circuits with coupled positive and negative feedback loops, Zhang *et al.* emphasized the reasons why a specific circuit topology exists in a cell, even though the same function could theoretically be achieved with an alternative architecture [77]. They also illustrated how distinct cis-regulatory modules fundamentally influence the cellular patterns of genetic oscillators, encompassing complete synchronization, diverse cluster-balanced states, and several cluster-nonbalanced states [78]. In our identified core structure [Fig. 2(c)], a positive feedback loop and negative feedback loop on the input node (topology M10) are essential for achieving the system's relaxation oscillation. In comparison to M10, oscillation probability significantly diminishes when considering the additional feedback of self-activation (M19) or self-inhibition (M14) of the output node [Fig. 1(c)]. Therefore, our analysis suggests that both positive and negative feedback of the output node can suppress the occurrence probability of oscillation, suggesting that additional feedback is not always beneficial to oscillation.

The essential structure for achieving biphasic dynamics has also been widely explored. We previously found the biphasic dynamics of PhoP phosphorylation regulated by PhoQ in bacteria [20], as well as the biphasic dynamics of CRY2 controlled by blue light in Arabidopsis [79]. In addition, the principle for the design of network topologies that robustly achieve adaptation, which is a typical biphasic behavior, was successfully dissected [42]. Here, we found the core structure that can simultaneously generate oscillation and biphasic dynamics, resulting in the BAD of oscillation. Oscillation is induced by the fast and slow dynamics of the two nodes, while biphasic dynamics of amplitude is determined by the linear and nonlinear responses of trough and crest. The observed mechanism of biphasic dynamics aligns with our most recent study on cell death signaling. We found that in necroptosis, RIP1 biphasically regulates RIP3 phosphorylation, and the underlying mechanism involves the linear and nonlinear recruitment of caspase-8 and RIP3 to necrosome [46]. These findings prompt further investigation to explore whether linear and nonlinear responses represent a generalizable design principle for robustly executing biphasic dynamics in biological systems.

Despite the apparent complexity of cell signaling networks, numerous studies have supported the idea that only a limited number of network topologies are capable of robustly executing particular biological functions. The topological design principles of natural capable of oscillation [36], adaptation [42] and self-organizing cell polarization [43] have been extensively studied. Considering the primary focus of this study is to investigate the topological design principles of BAD of oscillation, we thus proposed a phenomenological model based on well-established approaches used in previous studies [36,42,43], rather than a comprehensive biochemical reactions model to precisely evaluate each biological process. Our coarse-grained model is a phenomenological model that characterizes the regulatory relationship between signal nodes. Many intermediate products and reaction processes have been simplified and integrated into the model. When dealing with a specific biological system, it is essential to consider a comprehensive model that incorporates detailed biological reactions. Nevertheless, our conclusion regarding the identified essential topological structure for BAD of oscillation should hold in a general context. We hope our results can be found in an increasing number of future experimental observations.

Biological oscillation signals carry important information regarding both amplitude and period, enabling organisms to identify, encode, and transmit different biological information and execute various responses through oscillatory signaling [80,81]. Different types of oscillation signals selectively perform diverse biological functions. In the case of BAD, although amplitude is biphasically controlled, both trough and crest increase with the input strength. The topography of the landscape enables us to identify detailed dynamical properties of the system, such as the position and depth of the Mexican hat, and to further uncover the roles of input in regulating oscillation crest and trough. The recently developed non-Markovian theoretical modeling approach, opening up a new avenue of research [82], may also extend the generalizability of our results derived from the Fokker-Planck equation [Eq. (3)]. The landscapes depicted in Fig. 3(c) demonstrate diverse positions and sizes of the Mexican hat, leading to three distinct oscillation behaviors as illustrated in Fig. 4(c). Despite having similar amplitudes, the trough and crest at high input strengths are significantly larger than those at low strengths. An urgent question arises regarding how different oscillation behaviors can exert similar or distinct biological functions. Moreover, aside from BAD of oscillation, Stricker *et al.* observed the biphasic regulation of period by varying the Isopropyl ß-D-1-thiogalactopyranoside (IPTG) concentration in an oscillator of *Escherichia coli* [83]. The explicit mechanisms underlying the biphasic regulation of period is also a fundamental issue that needs to be explored in future research.

The ODE model is developed and simulated with PYTHON 3.8.2. Zipped mathematical code files of the model to generate the results in this study are available on GitHub [84].

ACKNOWLEDGMENTS

This work was supported by National Natural Science Foundation of China (Grant No. 12090052), Natural Science Foundation of Fujian Province of China (Grant No. 2023J05002), and the Fundamental Research Funds for the Central Universities (Grant No. 20720230017).

---

[1] P. E. Rapp, J. Exp. Biol. **81**, 281 (1979).
[2] J. W. Shuai and P. Jung, Phys. Rev. Lett. **88**, 068102 (2002).
[3] A. Weber, W. Zuschratter, and M. J. Hauser, Sci. Rep. **10**, 19714 (2020).
[4] L. Wettmann and K. Kruse, Philos. Trans. R. Soc., B **373**, 20170111 (2018).
[5] A. Goldbeter, *Biochemical Oscillations and Cellular Rhythms: The Molecular Bases of Periodic and Chaotic Behaviour* (Cambridge University Press, Cambridge, UK, 1997).
[6] E. Sel'Kov, Eur. J. Biochem. **4**, 79 (1968).
[7] A. Boiteux, A. Goldbeter, and B. Hess, Proc. Natl. Acad. Sci. USA **72**, 3829 (1975).
[8] M. Nakajima, K. Imai, H. Ito, T. Nishiwaki, Y. Murayama, H. Iwasaki, T. Oyama, and T. Kondo, Science **308**, 414 (2005).
[9] J. J. Tyson, Proc. Natl. Acad. Sci. USA **88**, 7328 (1991).
[10] J. E. Ferrell, Jr., T. Y.-C. Tsai, and Q. Yang, Cell **144**, 874 (2011).
[11] X. Li, Y. Wu, X. Gao, M. Cai, and J. Shuai, Phys. Rev. E **97**, 012406 (2018).
[12] Y. Chen, H. Qi, X. Li, M. Cai, X. Chen, W. Liu, and J. Shuai, Phys. Rev. E **94**, 022411 (2016).
[13] B.-W. Qin, L. Zhao, and W. Lin, Nat. Commun. **12**, 5894 (2021).
[14] L. Cai, C. K. Dalal, and M. B. Elowitz, Nature (London) **455**, 485 (2008).
[15] V. D. Longo and S. Panda, Cell Metab. **23**, 1048 (2016).
[16] N. Hao and E. K. O'shea, Nat. Struct. Mol. Biol. **19**, 31 (2012).
[17] J. Jodynis-Liebert and M. Kujawska, J. Clin. Med. **9**, 718 (2020).
[18] T. M. Varusai and L. K. Nguyen, Sci. Rep. **8**, 643 (2018).
[19] L. Mackay, N. Mikolajewicz, S. V. Komarova, and A. Khadra, Front. Physiol. **7**, 1 (2016).
[20] W. Liu, X. Li, H. Qi, Y. Wu, J. Qu, Z. Yin, X. Gao, A. Han, and J. Shuai, Bioinformatics **37**, 2682 (2021).
[21] D. Chen, Y. Xiong, L. Wang, B. Lv, and Y. Lin, Can. J. Physiol. Pharmacol. **90**, 455 (2012).
[22] M. Kaur, A. Ng, P. Kim, C. Diekman, and Y.-I. Kim, J. Biol. Rhythms **34**, 218 (2019).
[23] A. G. Chavan, J. A. Swan, J. Heisler, C. Sancar, D. C. Ernst, M. Fang, J. G. Palacios, R. K. Spangler, C. R. Bagshaw, S. Tripathi *et al.*, Science **374**, eabd4453 (2021).
[24] Y. M. Jeong, C. Dias, C. Diekman, H. Brochon, P. Kim, M. Kaur, Y.-S. Kim, H.-I. Jang, and Y.-I. Kim, J. Biol. Rhythms **34**, 380 (2019).
[25] A. C. Møller, A. Lunding, and L. F. Olsen, Phys. Chem. Chem. Phys. **2**, 3443 (2000).
[26] Q. Nai, H.-W. Dong, A. Hayar, C. Linster, and M. Ennis, J. Neurophysiol. **101**, 2472 (2009).
[27] N. Nada, E. Kolkaila, P. Schendzielorz, and T. El Mahallawi, Egypt. J. Otolaryngology **38**, 1 (2022).
[28] Y. Develle and H. Leblond, Front. Cell. Neurosci. **13**, 1 (2020).
[29] X. Liu, A. Chen, A. Caicedo-Casso, G. Cui, M. Du, Q. He, S. Lim, J. K. Hang, I. H. Christian, Y. Liu, Nat. Commun. **10**, 4352 (2019).
[30] F. R. Cross, N. E. Buchler, and J. M. Skotheim, Philos. Trans. R. Soc., B **366**, 3532 (2011).
[31] Z. Li, S. Liu, and Q. Yang, Cell Syst. **5**, 72 (2017).
[32] R. Milo, S. Shen-Orr, S. Itzkovitz, N. Kashtan, D. Chklovskii, and U. Alon, Science **298**, 824 (2002).
[33] O. Brandman, J. E. Ferrell, Jr., R. Li, and T. Meyer, Science **310**, 496 (2005).
[34] G. Hornung and N. Barkai, PLoS Comput. Biol. **4**, e8 (2008).

[35] B. Novák and J. J. Tyson, Nat. Rev. Mol. Cell Biol. **9**, 981 (2008).
[36] T. Y.-C. Tsai, Y. S. Choi, W. Ma, J. R. Pomerening, C. Tang, and J. E. Ferrell Jr., Science **321**, 126 (2008).
[37] Z.-B. Zhang, Q.-Y. Wang, Y.-X. Ke, S.-Y. Liu, J.-Q. Ju, W. A. Lim, C. Tang, and P. Wei, Cell Syst. **5**, 460 (2017).
[38] H. Qi, G. Xu, X.-L. Peng, X. Li, J. Shuai, and R. Xu, Phys. Rev. E **102**, 062422 (2020).
[39] C. del Junco and S. Vaikuntanathan, Phys. Rev. E **101**, 012410 (2020).
[40] M. Adler, P. Szekely, A. Mayo, and U. Alon, Cell Syst. **4**, 171 (2017).
[41] L. Goentoro, O. Shoval, M. W. Kirschner, and U. Alon, Mol. Cell **36**, 894 (2009).
[42] W. Ma, A. Trusina, H. El-Samad, W. A. Lim, and C. Tang, Cell **138**, 760 (2009).
[43] A. H. Chau, J. M. Walter, J. Gerardin, C. Tang, and W. A. Lim, Cell **151**, 320 (2012).
[44] Y. Li, Y. Jiang, J. Paxman, R. O. Richard, S. Klepin, Y. Zhu, L. Pillus, L. S. Tsimring, J. Hasty, N. Hao, Science **369**, 325 (2020).
[45] F. Xu, Z. Yin, L. Zhu, J. Jin, Q. He, X. Li, and J. Shuai, Front. Phys. **9**, 726638 (2021).
[46] X. Li, C. Q. Zhong, R. Wu, X. Xu, Z. H. Yang, S. Cai, X. Wu, X. Chen, Z. Yin, Q. He, D. Li *et al.*, Protein Cell **12**, 858 (2021).
[47] X. Li, P. Zhang, Z. Yin, F. Xu, Z. H. Yang, J. Jin, J. Qu, Z. Liu, H. Qi, C. Yao *et al.*, Research **2022**, 9838341 (2022).
[48] L. Zhu, X. Li, F. Xu, Z. Yin, J. Jin, Z. Liu, H. Qi, and J. Shuai, Q Chaos, Solitons Fractals **155**, 111724 (2022).
[49] L. Qiao, W. Zhao, C. Tang, Q. Nie, and L. Zhang, Cell Syst. **9**, 271 (2019).
[50] L. Oberreiter, U. Seifert, and A. C. Barato, Phys. Rev. E **106**, 014106 (2022).
[51] T. M. Varusai, W. Kolch, B. N. Kholodenko, and L. K. Nguyen, Mol. Biosyst. **11**, 2750 (2015).
[52] J. Shu *et al.*, Cell **153**, 963 (2013).
[53] R. L. Iman, J. C. Helton, and J. E. Campbell, J. Qual. Technol. **13**, 174 (1981).
[54] N. Eling, M. D. Morgan, and J. C. Marioni, Nat. Rev. Genet. **20**, 536 (2019).
[55] N. Engberg, M. Kahn, D. R. Petersen, M. Hansson, and P. Serup, Stem Cells **28**, 1498 (2010).
[56] X.-J. Tian, X.-P. Zhang, F. Liu, and W. Wang, Phys. Rev. E **80**, 011926 (2009).
[57] K. Maeda and H. Kurata, J. Theor. Biol. **440**, 21 (2018).
[58] S. Busenberg and P. Vandendriessche, J. Math. Anal. Appl. **172**, 463 (1993).
[59] N. S. Ginzburg, L. A. Yurovskiy, A. S. Sergeev, I. V. Zotova, and A. M. Malkin, Phys. Rev. E **104**, 034218 (2021).
[60] S. H. Strogatz, *Nonlinear Dynamics and Chaos: With Applications to Physics, Biology, Chemistry, and Engineering* (CRC Press, Boca Raton, FL, 2018).
[61] J. Wang, Adv. Phys. **64**, 1 (2015).
[62] J. Wang, L. Xu, and E. Wang, Proc. Natl. Acad. Sci. USA **105**, 12271 (2008).
[63] See Supplemental Material at http://link.aps.org/supplemental/10.1103/PhysRevE.108.064412 for more information about the content mentioned at the corresponding location in the text.
[64] G. Wang and C. S. Peskin, Phys. Rev. E **97**, 062416 (2018).
[65] J. R. Pomerening, E. D. Sontag, and J. E. Ferrell, Nat. Cell Biol. **5**, 346 (2003).
[66] K. Yagita *et al.*, Proc. Nat. Acad. Sci. USA **107**, 3846 (2010).
[67] T. Nagashima, H. Shimodaira, K. Ide, T. Nakakuki, Y. Tani, K. Takahashi, N. Yumoto, and M. Hatakeyama, J. Biol. Chem. **282**, 4045 (2007).
[68] D. Shin, I. S. Kim, J. M. Lee, S.-Y. Shin, J.-H. Lee, S. H. Baek, and K.-H. Cho, J. Mol. Cell Biol. **6**, 338 (2014).
[69] S.-Y. Shin, T. Kim, H.-S. Lee, J. H. Kang, J. Y. Lee, K.-H. Cho, and D. H. Kim, Nat. Commun. **5**, 5777 (2014).
[70] X. Li, J. Jin, X. Zhang, F. Xu, J. Zhong, Z. Yin, H. Qi, Z. Wang, and J. Shuai, npj Syst. Biol. Appl. **7**, 35 (2021).
[71] Y. Zhao, D. D. Wang, Z. W. Zhang, Y. Lu, X. J. Yang, Q. Ouyang, C. Tang, and F. T. Li, Phys. Rev. E **101**, 042405 (2020).
[72] U. Alon, *An Introduction to Systems Biology: Design Principles of Biological Circuits* (Chapman and Hall/CRC, London, 2006).
[73] L. Qiao, Z.-B. Zhang, W. Zhao, P. Wei, and L. Zhang, eLife **11**, e76188 (2022).
[74] S. M. Castillo-Hair, E. R. Villota, and A. M. Coronado, Syst. Synth. Biol. **9**, 125 (2015).
[75] X.-P. Zhang, F. Liu, and W. Wang, Proc. Natl. Acad. Sci. USA **108**, 8990 (2011).
[76] L.-S. Wang, N.-X. Li, J.-J. Chen, X.-P. Zhang, F. Liu, and W. Wang, Phys. Rev. E **97**, 042412 (2018).
[77] J. Zhang, Z. Yuan, H.-X. Li, and T. Zhou, Biophys. J. **99**, 1034 (2010).
[78] J. Zhang, Z. Yuan, and T. Zhou, Phys. Rev. E **79**, 041903 (2009).
[79] Y. Wu, Q. Wang, J. Qu, W. Liu, X. Gao, X. Li, X. Ouyang, C. Lin, and J. Shuai, Plant Cell Environ. **44**, 1802 (2021).
[80] A. M. Corrigan and J. R. Chubb, Curr. Biol. **24**, 205 (2014).
[81] P. Paszek, D. A. Jackson, and M. R. H. White, Curr. Opin. Genet. Dev. **20**, 670 (2010).
[82] J. Zhang and T. Zhou, Proc. Natl. Acad. Sci. USA **116**, 23542 (2019).
[83] J. Stricker, S. Cookson, M. R. Bennett, W. H. Mather, L. S. Tsimring, and J. Hasty, Nature (London) **456**, 516 (2008).
[84] https://github.com/little-jun/BAD-main.